PHYSICAL REVIEW B VOLUME 45, NUMBER 9 1 MARCH 1992-I

Nanocrystalline Fe-(Co,Ni)-Si-B: The mechanical crystallization of amorphous alloys and the effects on electrocatalytic reactions

M. L. Trudeau, J. Y. Huot,* and R. Schulz
Technologie des Matériaux, Institut de Recherche d'Hydro-Québec, Varennes, P.Q., Canada J3X 1S1

D. Dussault and A. Van Neste
Département de Mines et Métallurgie, Université Laval, Québec, P.Q., Canada G1K 7P4

G. L'Espérance
Département de Métallurgie et Génie des Matériaux, Ecole Polytechnique Montréal,
P.Q., Canada H3C 3A7

(Received 6 May 1991; revised manuscript received 24 October 1991)

We have studied the process of mechanical crystallization on amorphous Fe-(Co,Ni)-Si-B metallic powders. Under high-energy mechanical deformations, these alloys crystallize into a nanocrystalline structure. The presence of Co accelerates the crystallization kinetics, while Ni slows it down. The dynamical equilibrium between crystal growth and fracture of the crystallites by the mechanical deformations gives rise to a distribution of crystal sizes whose average value is localized between 8 and 10 nm. The electrocatalytic activity of these nanocrystalline materials for the hydrogen evolution reaction in alkaline solutions is related to the presence of extremely small α-iron crystallites. The mechanical crystallization process can be used effectively for producing highly electroactive metastable materials.

I. INTRODUCTION

Nanocrystalline solids (NS) have been the subject of several discussions in the literature.[1,2] These materials are made of extremely small crystals ranging from 1 to 10 nm. Due to the size of the crystallites, about 50% of the volume of the material is composed of crystalline interfaces and grain boundaries. For this reason some researchers have suggested that these solids have two different local atomic structures: the standard one, typical of crystals with long-range order, for all the atoms far from any boundaries, and a disordered structure with only short-range order for the interfacial regions.[1,2] The large amount of disorder at the interfaces has led some authors to suggest that the grain-boundary regions are gaslike in nature.[2,3] Others argue that they should be more liquidlike or of the type found in normal coarser-grain materials.[1] Moreover, not only do they possess a unique microstructure; these solids also have very interesting physical and chemical properties. In particular, it has been suggested that the catalytic activity can increase greatly when an alloy is made into a nanocrystalline form.[2]

Up to now, nanocrystalline solids were produced by three different techniques. The first uses the evaporation in a high-purity noble-gas atmosphere followed by a condensation process.[3] A second method consists of heat treating some amorphous alloys at low temperatures. For example, Thorpe *et al.*[4] produced a partially crystalline material with crystal sizes ranging from 2 to 15 nm by annealing an amorphous $Fe_{32}Ni_{36}Cr_{14}P_{12}B_6$ alloy for 2 months at a temperature well below the crystallization temperature. Recently Yoshizawa *et al.*[5] have shown that, by alloying some amount of Cu and Nb into an amorphous FeSiB ribbon, the growth process of the α-iron phase during thermal crystallization is slowed down; the average crystal size always remains below 10 nm. Finally, a third technique is the high-energy mechanical deformation process. Hellstern *et al.*[6,7] have produced AlRu powders with crystals of about 7 nm by milling the crystalline intermetallic compound for 64 h. Another example is the production of nanocrystalline NiMo alloys by high-energy mechanical alloying of the elemental components.[8,9] Moreover, these metastable NiMo alloys exhibit an extremely high electrocatalytic activity for the hydrogen evolution reaction in alkaline solutions.[10]

Recently, the high-energy mechanical deformations technique has also been used to crystallize amorphous metallic alloys.[11] In the present investigation, the crystallization by mechanical deformations of several amorphous iron-based alloys is studied and compared to the more familiar thermal crystallization process. We show that the competition between the crystal growth and the fracture mechanism, due to the accumulation of internal strain in the crystals, gives rise to a distribution of α-iron crystals with an average size remaining below 10 nm. The crystal growth mechanism is investigated for both stages of the crystallization.

Since small iron particles have previously demonstrated good electrocatalytic activities for the hydrogen evolution reaction in alkaline solutions,[12,13] the process of mechanical crystallization may turn out to be an efficient method for producing active catalysts. Indeed, by reducing the size of the particles to the nanometer scale, it may be possible to increase the activity of the materials. We have thus studied the electrocatalytic properties of the nanocrystalline electrodes made by cold pressing the mechanically crystallized powders and the results have been compared to the properties of the amorphous and thermally crystallized ribbons.

II. EXPERIMENTAL DETAILS

The investigated alloys are listed in Table I. The amorphous alloys were made by the standard melt-spinning technique. Two of them, the $Fe_{78}Si_9B_{13}$ (Metglas 2605S-2) and the $Fe_{66}Co_{18}Si_1B_{15}$ (Metglas 2605CO) were bought directly from Allied Metglas Products. The $Fe_{58}Co_{26}Si_9B_7$ alloy could not be made completely amorphous by melt spinning and therefore sample H is partially crystalline. The amorphous nature of the ribbons was checked by a Philips x-ray diffractometer equipped with a graphite monochromator and using Mo $K\alpha$ radiation. Samples containing less than 1% of crystals were classified as amorphous.

The nanocrystalline powders were produced by high-energy ball milling using a SPEX 8000 laboratory mixer and a 70-ml steel vial with two $\frac{1}{2}$ in.- and one $\frac{9}{16}$ in.-diam steel balls. The samples were made by milling pieces of amorphous ribbons of Metglas 2605S-2 or Metglas 2605CO with and without the addition of pure Co or Ni in order to obtain the desired average chemical composition. The pure metals alloy with the amorphous phase very rapidly at the beginning of the milling process.[11] The Ni powder was 99.9% pure and the size of the particles was around 100 μm while Co was 99.8% pure with a particle size of about 75 μm. The ball to powder weight ratio was always kept near 4:1. The vial was sealed in a glove box under an argon inert atmosphere.

Chemical analysis of the alloys was performed on a scanning electron microscope by energy dispersive x-ray (EDX) analysis using a Tracor Northern detector and the Metglas ribbons as standards. Chemical analysis was also performed by Auger spectroscopy using a Perkin Elmer Phi-660 instrument. Thermal stability, up to 600 °C, was monitored by differential scanning calorimetry using a DSC-4 from Perkin-Elmer. The oxygen and nitrogen content of the powder was measured by a Leco O_2-N_2 detector. A Hitachi H-9000 scanning transmission electron microscope, operating at 300 kV, was used to study the microstructure of the powders. Samples for transmission electron microscopy (TEM) were made by simply pressing some powder onto a copper grid. The image analysis was made on a Tracor Northern 8500 analyzer coupled to a Gatan image intensifier located below the phosphorus screen in the microscope. A JEOL 2000FX TEM operating at 200 kV and equipped with a Link ultrathin window x-ray detector was used to analyze the crystalline products after thermal crystallization of the amorphous ribbons.

For the electrochemical reaction, the ribbons were cut into pieces and spark welded onto a support while the powders were consolidated into a pellet (0.95 cm in diameter) using a pressure of $\sim 10\,000$ kg/cm^2 and mechanically bonded to the electrode support. The electrochemical cell consists of a nanocrystalline cathode (the working electrode, W), a nickel anode (the counter electrode, CE) (99.99% MRC) and an external Hg-HgO-KOH 1M reference electrode (REF). Figure 1 shows a schematic diagram of the electrochemical cell and electronic circuit. All potentials are given with respect to the reference electrode. The reversible potential, $E_{\rm rev}$, for the hydrogen evolution reaction in 30 wt % KOH at 70 °C is -0.960 V. For larger (more negative) potentials, hydrogen gas evolves from the surface of the cathode. The working electrode potential or the current between the anode and the cathode was controlled by a 1286 electrochemical interface from Solartron.

For the ribbons, *in situ* oxidations were performed at 1 mA cm^{-2} for 10^4 s prior to the hydrogen discharge in order to activate the electrode. This procedure was not necessary in the case of the powder pellets.

The performance of the nanocrystalline cathodes with respect to the hydrogen evolution reaction is primarily characterized by the hydrogen overpotential which is given by the working electrode potential (measured with respect to the reference electrode) minus the reversible potential and the ohmic drop (RI), where R is the ohmic resistance. A linear relationship exists between the hydrogen overpotential η and the cathodic current density i:

$$\eta = a + b \log_{10}(i) = E - RI - E_{\rm rev} \ ,$$

TABLE I. Alloys and electrocatalytic parameter measured at 250 mA cm^{-2} in 30 wt % KOH at 70 °C. *a* represents amorphous; *n*, nanocrystalline powder; *c*, partially crystallized ribbon.

	Alloys composition	Milling time h	Geometry of the electrode	Crystal size Å	Strain %	Overpotential mV	Exchange current mA cm^{-2}	Taffel slope mV
A	a-$Fe_{78}(Si_9B_{13})$		Oxy-red ribbon			300	1.2	130
B	a-$Fe_{72}Co_8(Si_{12}B_8)$		Oxy-red ribbon			385	0.61	147
C	n-$Fe_{68}Co_{16}(Si_7B_9)$	6	Consolidated powder	40	0.83	212	0.21	69
D	a-$Fe_{66}Co_{18}(Si_1B_{15})$		Oxy-red ribbon			185	0.3	64
E	n-$Fe_{63}Co_{20}(Si_7B_{10})$	8	Consolidated powder	55	0.78	164	1.3	72
F	a-$Fe_{60}Co_{20}(Si_{10}B_{10})$		Oxy-red ribbon			157	2.3	77
F^*	a-$Fe_{60}Co_{20}(Si_{10}B_{10})$		Ribbon no oxy-red			385	0.4	13
G	n-$Fe_{58}Co_{26}(Si_7B_9)$	24	Consolidated powder	89	1.06	181	0.82	73
H	c-$Fe_{58}Co_{26}(Si_9B_7)$		Oxy-red ribbon	225	0.08	286	1.7	132
I	a-$Fe_{65}Ni_{17}(Si_{11}B_7)$		Oxy-red ribbon			390	0.14	122
J	a-$Fe_{65}Ni_{17}(Si_7B_{11})$	24	Consolidated powder			231	0.25	77

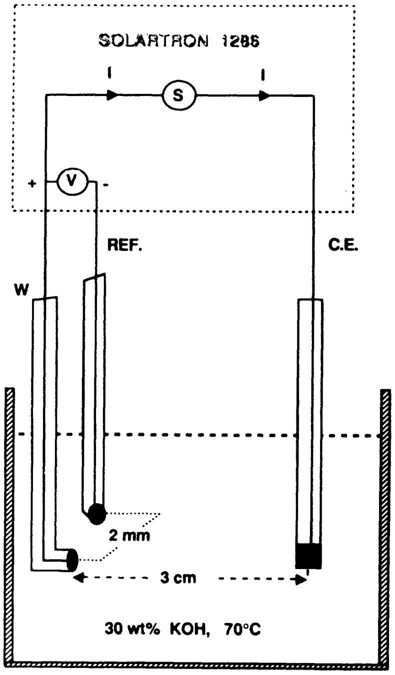

FIG. 1. Schematic diagram of the electrochemical cell and electronic circuit.

where a and b are constants. The current, I, versus potential, E, curves were recorded between -1.3 and -1.0 V after keeping the working-electrode potential at -1.3 V for 10^4 s. The data were fitted with the above equation to get the values of the Tafel slope, b, the extrapolated current density at the reversible potential, or the exchange current density, $i_0=10^{-a/b}$, as well as the ohmic resistance factor, R. From the value of i_0 and b, we can calculate the overpotential at 250 mA cm^{-2}

$$\eta_{250}=b\log_{10}(250/i_0)\ .$$

The overpotential at 250 mA cm^{-2} is used to characterize the performance of the electrodes. The best electrodes are the ones with the lowest overpotential. The Tafel slope, which is related to the mechanism of the reaction, must also be as small as possible. It represents the increase in potential needed to increase the current density by a factor of 10. Finally, the electrodes with the highest exchange current densities are usually the ones having the largest effective surface areas when the Tafel slopes are equal.

III. RESULTS AND DISCUSSION

A. Structural transformations

1. *Thermal crystallization*

During thermal treatments, the

$$\mathrm{Fe}_{80-x}(\mathrm{Co,Ni})_x(\mathrm{Si,B})_{20}$$

metallic glasses crystallize usually in two steps. A primary crystallization of α-iron followed by the crystallization of a boride phase. For example, Fig. 2(a) shows a TEM micrograph of a fully crystallized ribbon of $Fe_{60}Co_{20}Si_{10}B_{10}$. Electron diffraction and energy dispersive x-ray analysis reveal the presence of two different phases. The diffraction patterns obtained from the grains shown in Fig. 2(a) can be indexed to α-iron with $a=0.2840$ nm and to a body-centered-tetragonal (bct) phase with $a=b=0.5097$ and $c=0.4237$ nm. The schematic patterns showing the indices of the reflections and the zone axis are presented in Figs. 2(b) and 2(c) for both grains. The EDX spectrum of the α-iron phase indicates that it contains cobalt and silicon in solution. Since the solubility of boron in α-iron is less than 0.1%,[14] it has been possible to calculate the composition by using calibration factors (k_{AB}) measured on the $Fe_{60}Co_{20}Si_{10}B_{10}$ alloy in the amorphous state.[15] The composition of the α-iron phase obtained using this procedure was $Fe_{60}Co_{26}Si_{14}$. In the case of the bct boride phase, the EDX analysis showed some cobalt and a relatively small amount of silicon. The boron was not detected because of the absorption of the low-energy x rays (0.185 keV). Quantification using the appropriate calibration factors gives $Fe_{58}Co_8Si_1B_{33}$ assuming a boron to metal ratio of 1B:2[Fe,Co,Si]. The lattice parameters measured by electron diffraction and confirmed by previous x-ray analysis[13] are within 5% of those of Fe_2B.

2. *Mechanical crystallization*

Fe-Si-B metallic glasses also crystallize when they are subjected to a mechanical deformation.[11] Since it is a low-temperature process, the growth of the crystalline phase is taking place at a very slow rate. Moreover, once the crystals are formed, they are fractured into smaller pieces and therefore the crystals never reach sizes above 10 nm. The addition of Co to the amorphous alloy during the milling process accelerates the crystallization. The phase which forms first is, as in the thermal process, the α-Fe(Co,Si) followed, after a longer milling time, by the $(Fe,Co,Si)_2B$ structure. The addition of Ni, on the contrary, stabilizes the amorphous structure and slows down the crystallization process. No crystalline phase can be seen by x-ray diffraction in the $Fe_{65}Ni_{17}Si_7B_{11}$ alloy (sample J) up to 24 h of milling. Figure 3 shows the x-ray patterns of samples C, E, G, and J after milling. All the samples containing Co show the presence of crystalline phases while the one with Ni appears amorphous.

Using the full width at half-maximum of the x-ray peaks, it is possible to obtain, after correction for $K\alpha_2$ and instrumental broadening, the values of the average crystal size and the internal rms strain. To a first approximation, the broadening due to the small crystal size and the rms strain is given by[16]

$$\Delta K=1.8\pi/d+A\langle e^2\rangle^{1/2}K\ ,$$

where d is the average size of the crystallites, $\langle e^2\rangle^{1/2}$ is the rms strain and A is a constant related to the strain distribution. This constant can be approximated to 1 for a random distribution of dislocations.[16] Four reflections were used to characterize the α-iron structure: the (110), (200), (220), and (321). The other lines in the spectra [(211) and (310)] were rejected because of the potential interference with the second crystalline phase $(Fe,Co,Si)_2B$.

Figure 4(a) shows the average size of the α-iron crystallites in a $Fe_{66}Co_{18}Si_1B_{15}$ amorphous alloy as a function of the milling time. The size increases from about 3.5 nm after 4 h of milling to approximately 9.0 nm after 30 h. In parallel, Fig. 4(b) shows the rms strain in the crystallites as a function of the milling time. The first crystals have basically no internal strain. As they grow, the strain increases up to a limit of about 1.25%. When this critical value is reached, the crystals break and the strain is released. With further milling the size increases again, as well as the strain, up to the same upper limit. The straight line in Fig. 4(a) represents a $\sqrt{t}$ variation which indicates that the growth of the α-Fe crystals is controlled by a diffusion process.

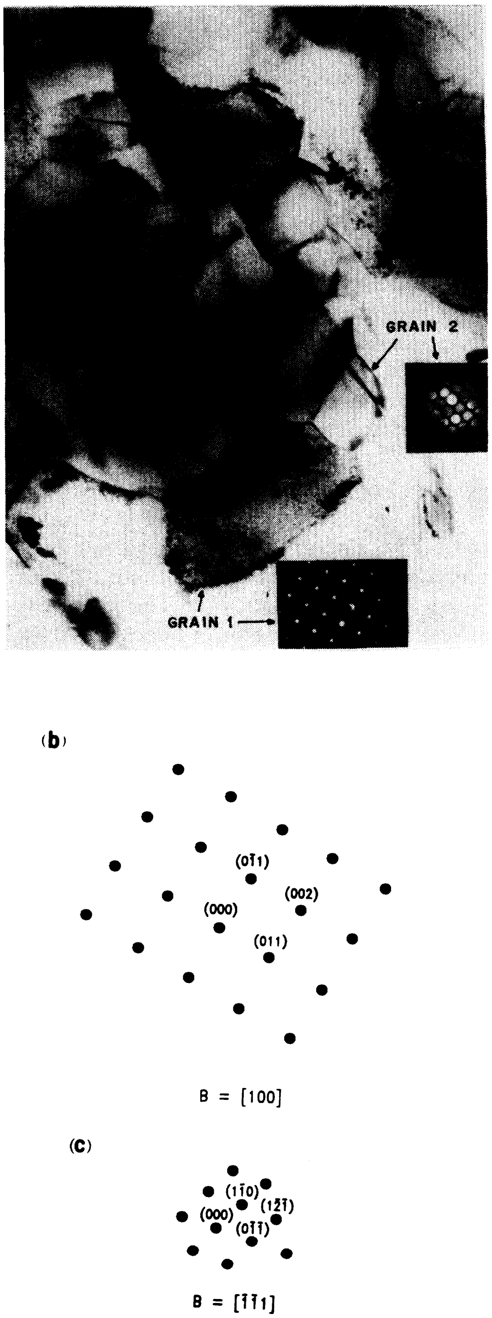

FIG. 2. (a) TEM micrograph of crystalline $Fe_{60}Co_{20}Si_{10}B_{10}$ alloy. (b) and (c) Schematic diffraction patterns of the grains shown in (a).

During the milling, when a crystalline phase grows, the corresponding differential scanning calorimetry (DSC) peak associated with the thermal crystallization of that phase decreases in proportion. For the Metglas 2605CO ($Fe_{66}Co_{18}Si_1B_{15}$), the first DSC peak which corresponds to the crystallization of α-iron, disappears in the first 5 h of milling. The second peak shifts to lower temperatures at the beginning of the process and decreases in intensity afterwards. Figure 5 shows the normalized crystalline fraction, V_c/V_T, as a function of milling time calculated from the changes in the area of the corresponding DSC peaks. The solid lines are least-squares fits using the Avrami's expression describing an isothermal structural transformation:[17]

$$V_c/V_T = 1 - \exp[-(kt)^n] \ .$$

In this equation, the rate constant k is function of the temperature and depends on the nucleation rate and on the speed of growth of the crystallites. n is the Avrami's exponent which is related to the growth mechanism.[17] For the α-iron phase, the parameters obtained from the fit are $k = 0.372h^{-1}$ and $N = 1.46$. For the bct boride phase $k = 0.016h^{-1}$ and $n = 1.43$. Since the α-iron structure is boron free and the growth of the crystallites follows a $\sqrt{t}$ law, it seems, therefore, that the diffusion of boron controls the first stage of the mechanical crystallization process as in the case of the thermal crystalliza-

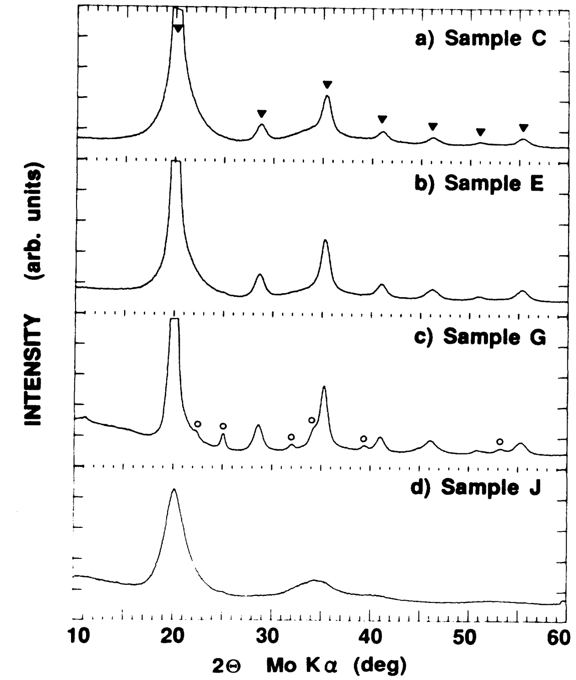

FIG. 3. Diffraction patterns of (a) $Fe_{68}Co_{16}Si_7B_9$ milled for 6 h (sample C), (b) $Fe_{63}Co_{20}Si_7B_{10}$ milled for 8 h (sample E), (c) $Fe_{58}Co_{26}Si_7B_9$ milled for 24 h (sample G), and (d) $Fe_{65}Ni_{17}Si_7B_{11}$ milled for 24 h (sample J). (▼) α-Fe and (○) Fe_2B structure.

tion.[18] According to Christian,[17] a value of the exponent of 1.5 indicates a zero-nucleation rate and crystals growing in all shapes from very small dimensions. A value of n near 1.5 is also obtained for the second crystalline product indicating that the same mechanism may apply to both phases.

To get a better understanding of the mechanical crystallization mechanism, we have also evaluated, using thermal experiments, the values of Avrami's exponent of the powders after various milling times. Using the values of the activation energy E_a obtained previously[11] (2.2 and 3.5 eV for the first and second crystallization process, respectively) and the data from the isochronal heating experiments, Avrami's exponent can be calculated using Piloyan's procedure:[19]

$$\frac{d\ln\Delta H}{d(1/T)}=\frac{-nE_a}{k_B}\ ,$$

where ΔH is the amount of heat released at a temperature T at the beginning of the thermal crystallization. Figures 6(a) and 6(b) show the $\log_{10}(\Delta H)$ versus $1000/T$ for both DSC peaks as a function of the milling time. For the amorphous ribbon (0 h) the exponents are 1.5 for the crystallization of α-iron and 3.5 for Fe_2B. From isothermal experiments, Jones *et al.*[18] found that Avrami's exponent for the crystallization of α-iron changes from 1.5 to 0.5 during the precipitation process. This may explain the strong curvature observed in Piloyan's traces of Fig. 6(a). Figures 6(a) and 6(b) reveal that the thermal crystallization of both phases is significantly modified by the mechanical deformations. It is, however, for the crystallization of $(Fe,Co,Si)_2B$ that the impact of the milling is the greatest. For this crystalline phase, the initial exponent of 3.5 decreases to 1.5 after 4 h of milling and to 0.5 after 15 h.[20] The milling modifies the microstructure of the alloy in such a way that the conditions for thermal crystallization change drastically. The initial exponent of 3.5 for the amorphous ribbon indicates that the crystals grow in all shapes from small dimensions with an increasing nucleation rate. After several hours of milling, the

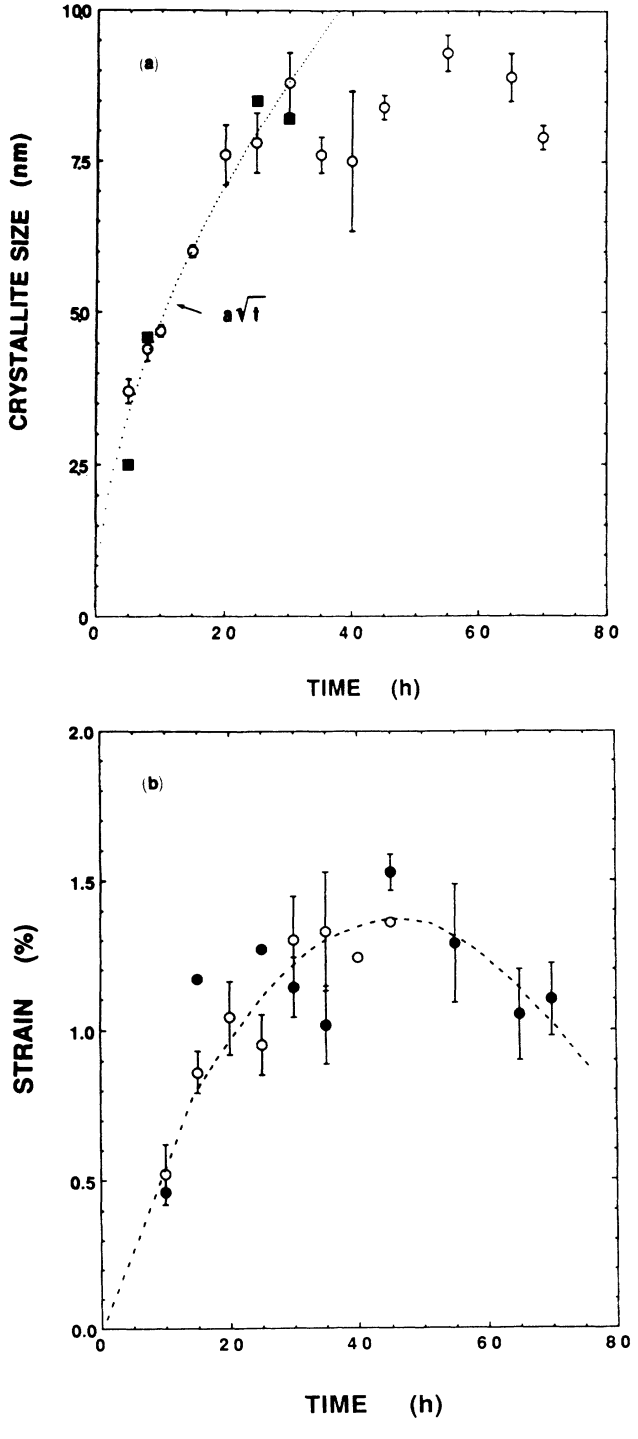

FIG. 4. (a) Average crystallite size in $Fe_{66}Co_{18}Si_1B_{15}$ amorphous alloy as a function of milling time measured from (○) x-ray-diffraction and (■) TEM observations; the dotted line represents a $\sqrt{t}$ variation. (b) rms strain in the crystalline.

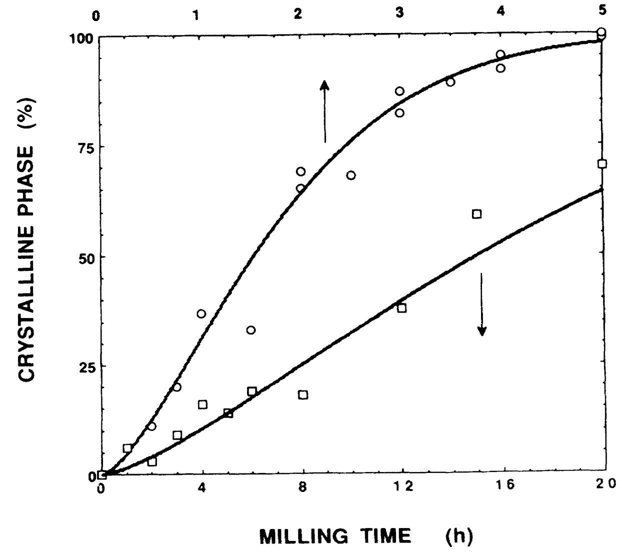

FIG. 5. Normalized volume fraction of the (○) α-Fe and (□) Fe_2B crystals as a function of the milling time. The solid lines correspond to a fit of the data.

microstructure is lamellar,[21] a large number of defects have been created and most nucleation sites have been formed. At this point, thermal crystallization becomes a one-dimensional growth from a fixed number of nuclei like in the thickening of crystalline platelets with possibly some precipitation on dislocations or other structural defects. According to Christian,[17] the value of n in this case is around 0.5, in agreement with the experimental results.

We should point out that the contamination of the powder by oxygen or other metallic impurities from the milling tools may also have an influence on the structural transformations.[22,23] Detailed elemental analysis, using energy dispersive x-ray techniques, have indicated an increase in the Fe and Cr content by about 3 at. % after 65 h of milling. The oxygen content increases typically by 0.5 and 1.0 wt % after 25 and 50 h of milling, respectively.

The microstructure of the ball-milled $Fe_{66}Co_{18}Si_1B_{15}$ alloy was also investigated by transmission electron microscopy. Figures 7(a) and 7(b) show bright-field TEM micrographs with its corresponding diffraction pattern for an alloy after 3 h of milling. We observe a distribution of very small crystallites highly dispersed into the amorphous matrix. The mostly complete rings are characteristic of the presence of numerous randomly oriented crystals. The average size of the crystallites is about 2.5 nm. With increasing milling time, the volume fraction of the crystalline phase as well as the size of the precipitates increase as shown in Figs. 8(a) and 8(b) taken after 8 and 25 h of milling, respectively. The alloy is completely crystalline after 25 h. In this picture we can observe a large number of grain boundaries and crystalline interfaces which are typical of nanocrystalline solids. We can also distinguish numerous moiré fringes coming from the superposition of the nanocrystals. A detailed discussion of the structural defects and grain boundaries in these materials has been published elsewhere.[24] The size distribution of the crystallites after 5 and 25 h of milling is shown in Figs. 9(a) and 9(b), respectively. These distributions were obtained by analyzing dark-field micrographs. The average size of the crystallites measured by TEM is in good agreement with the one estimated from the x-ray diffraction analysis [Fig. 4(a)].

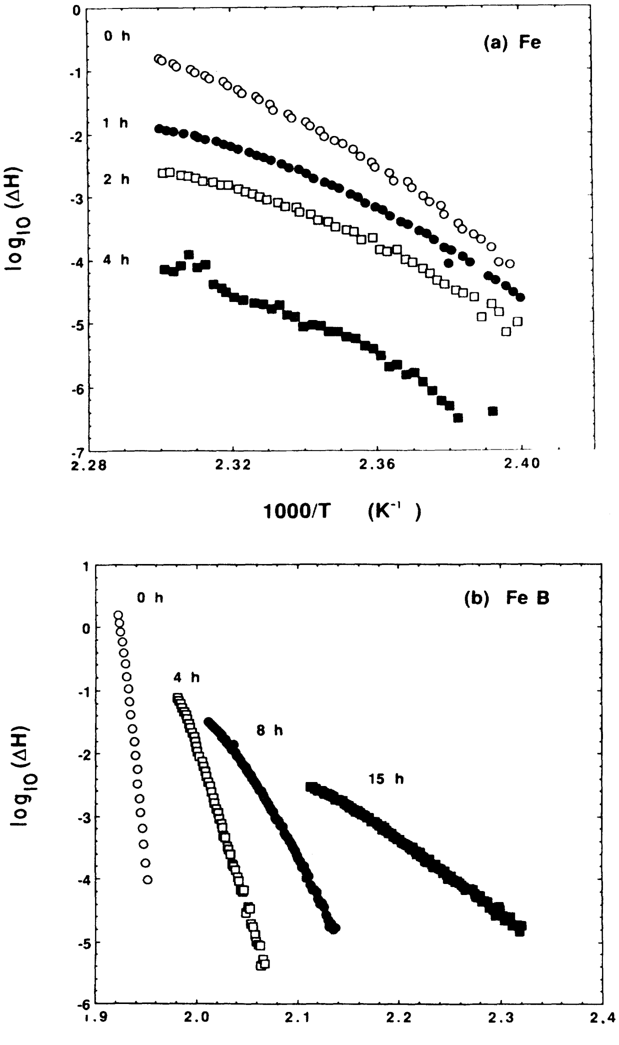

FIG. 6. log of the heat released as a function of 1000/T for (a) α-Fe and (b) Fe_2B after various milling times.

We have also investigated the $Fe_{65}Ni_{17}Si_7B_{11}$ powder after 24 h of milling. The x-ray diffraction pattern shown in Fig. 3(d) reveals only the presence of the amorphous phase. The TEM dark-field images, however, of Fig. 10 indicate that some crystallites are present but that their size and volume fraction are quite small compared with those of the Co-based alloys after the same milling time. Significant crystallization of this compound by mechanical deformations occurs only after about 100 h of milling.

B. Electrocatalytic properties

The electrocatalytic properties of nanocrystalline powders for the hydrogen evolution reaction in alkaline solutions (30 wt % KOH) have been investigated at 70 °C. The $Fe_{60}Co_{20}Si_{10}B_{10}$ alloy (sample F^* in Table I) was studied in great detail.[12,13] In the as-prepared state, this amorphous alloy is not electroactive. The hydrogen overpotential is 385 mV and the exchange current density is 0.4 mA cm^{-2}. An *in situ* oxidation-reduction treatment improves, however, the performance of the electrode. The oxidation leads to the formation of an Fe_3O_4 surface layer which reduces to pure Fe after cathodic reduction. The surface morphology of the active ribbon electrode consists in a distribution of small iron particles with a size of about 100 nm. These iron crystallites were found to be responsible for the electrocatalytic activity.

Table I lists the electrocatalytic parameters for the hydrogen evolution reaction of all the amorphous and nanocrystalline alloys. Apart from sample F^*, all the amorphous ribbons were activated by the previously described anodic oxidation treatment prior to the hydrogen discharge. Without it, any of the bare amorphous alloys were electroactive. The nanocrystalline powder pellets, however, were used without any prior treatment.

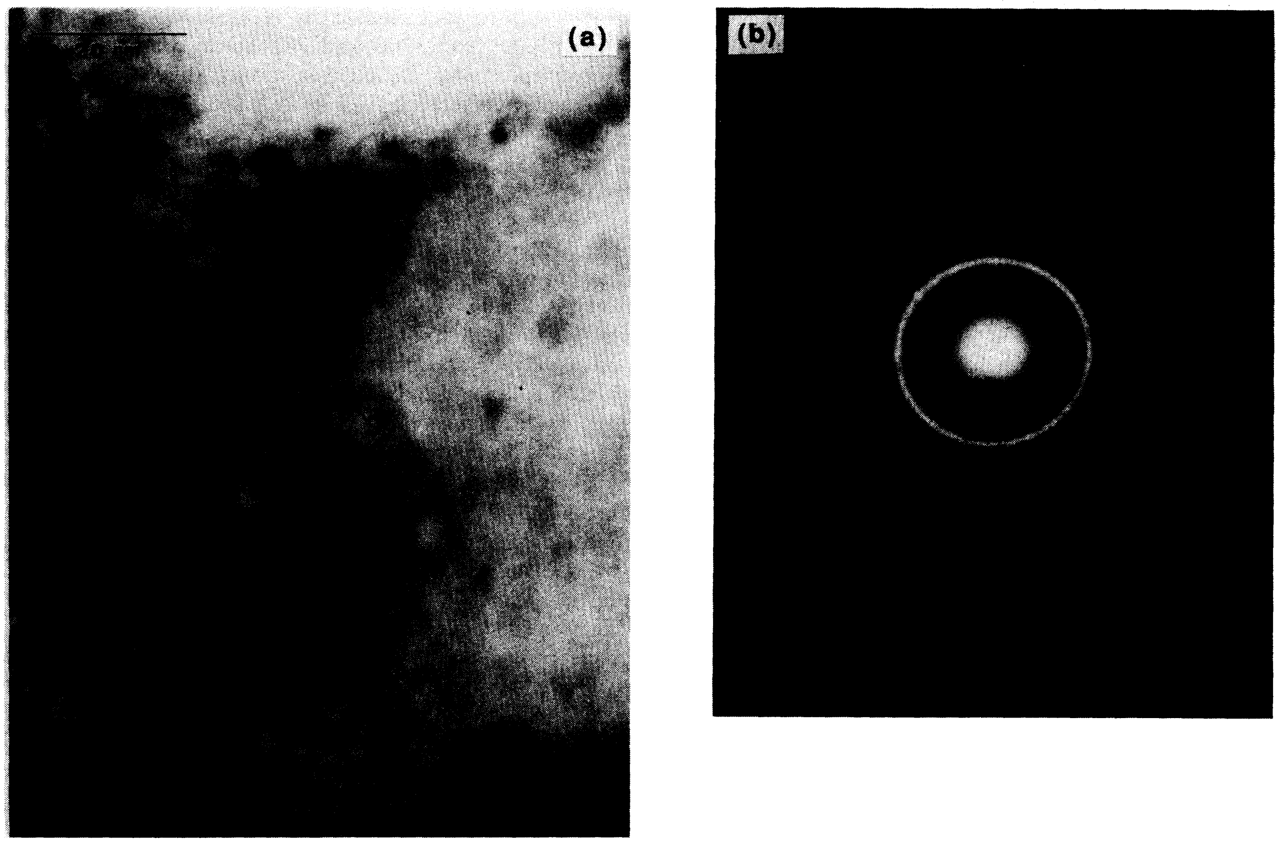

FIG. 7. (a) Bright-field micrographs and (b) electron-diffraction pattern of $Fe_{66}Co_{18}Si_1B_{15}$ after 3 h of milling.

The electrocatalytic properties of the nanocrystalline alloys are comparable to those of the amorphous ribbons with the same chemical composition after the oxidation-reduction treatment. This is not surprising since, in both cases, the material contains α-iron crystallites. Indeed the oxidation-reduction treatments as well as the mechanical crystallization process lead to the formation of very small α-iron crystallites. A difference exists, however, in the amount of elements in solution in both phases. The oxidation reduction leads to the formation of pure iron at the surface while Co and Si are present in the α-iron nanocrystals formed by mechanical crystallization.

1. Treated amorphous ribbons

The addition of Co to the amorphous Fe-Si-B alloys decreases the overpotential from the initial value of about 350 mV [300 mV for sample *A* (0% Co) and 385 mV for sample *B* (8% Co)] to a value as low as 157 mV for the alloy containing 20 at. % Co (sample *F*). The overpotential of the alloy with 26 at. % Co (sample *H*, 286 mV) is higher probably because it cannot be made completely amorphous by the melt-spinning technique. Indeed, a similar deterioration in the performance of the electrode was observed for the partially crystallized $Fe_{60}Co_{20}Si_{10}B_{10}$ alloy.[13] The reason for this being that the *in situ* oxidation reduction process leads to a smaller average particle size and a more homogeneous particle-size distribution in the case where the initial metallic support is totally amorphous.

Since the chemical composition of the iron surface layer is basically identical for each ribbon, the amplitude of the exchange current density is directly related to the effective surface area involved in the electrocatalytic reaction. Sample *F* ($Fe_{60}Co_{20}Si_{10}B_{10}$) has the largest exchange current density (2.3 mA cm^{-2}) and the best electrocatalytic properties. Its surface morphology is shown in Fig. 11(a). Sample *B*, with 8 at. % of Co, and sample *D*, with 18 at. % of Co and much less Si, have a

TABLE II. Value of the electrocatalytic parameters for two powder electrodes after anodic oxidation *a* represents amorphous and *n* represents nanocrystalline.

E	*n*-$Fe_{63}Co_{20}(Si_7B_{10})$	1	5000	167	0.61	64
		10	5000	154	0.83	62
J	*a*-$Fe_{65}Ni_{17}(Si_7B_{11})$	1	5000	187	1.6	96
		10	5000	211	2.2	91

significantly lower exchange current density. Their surface morphologies are shown in Figs. 11(b) and 11(c), respectively. They both have much coarser particle-size distributions. The Co as well as the Si content have, therefore, a direct influence on the electrochemical oxidation-reduction processes.

The sample containing Ni ($Fe_{65}Ni_{17}Si_{11}B_7$, sample *I*) behaves differently. The oxidation-reduction processes do not lead to the formation of a microcrystalline iron surface layer. Figure 11(d) shows a featureless scanning electron microscopy (SEM) micrograph of the surface of this alloy after treatment. The Auger depth profile (Fig. 12) indicates that a Ni oxide layer, about 30 nm thick, has been formed at the end of the anodic oxidation process, when the electrode potential reached the oxygen evolution potential. This sample has the worst catalytic properties. The overpotential is 390 mV and the exchange current density is 0.14 $mA\,cm^{-2}$.

2. *Nanocrystalline powder electrodes*

The nanocrystalline powder electrodes show good catalytic properties without the need of a prior oxidation treatment. This is related to the fact that the mechanical deformation process transforms directly the amorphous alloy into an active nanocrystalline structure. Among all the investigated alloys, the 24-h milled $Fe_{65}Ni_{17}Si_7B_{11}$ sample (*J*) has the worst electrocatalytic activity. As mentioned before, this sample stays amorphous upon milling. The overpotential is 231 mV and the exchange current density of 0.25 $mA\,cm^{-2}$ is rather low. Its overall performance, however, is better than that of the amorphous ribbon counterpart, probably because of the absence of a passive Ni oxide layer and the presence of some very small iron crystallites.

All the Co-based nanocrystalline powder electrodes have good electrocatalytic properties. After only 6 h of milling, the average size of the α-iron crystallites is very small (about 3.5 nm) and there is still a substantial volume fraction of amorphous phase present in the material. For these reasons, the $Fe_{68}Co_{16}Si_7B_9$ powder electrode (sample *C*) shows a relatively small exchange current density (0.21 $mA\,cm^{-2}$) but already a slightly better hydrogen overpotential (212 mV). With increasing milling time or Co content, the volume fraction of the nanocrystalline phase increases. The $Fe_{63}Co_{20}Si_7B_{10}$ powder electrode (sample *E*) milled for 8 h shows a very low hydrogen overpotential (164 mV) and a high exchange current density (1.3 $mA\,cm^{-2}$). The size of the α-iron crystallites after such a period of time is about 4.5 nm. For longer milling times, the increase in the size of the crystallites and the volume fraction of the boride phase reduce the effective catalytic surface. Sample *G*, in Table I, shows the catalytic properties of $Fe_{58}Co_{26}Si_7B_9$ after 24 h of milling. The crystal size has reached its equilibrium value of about 9.5 nm, the overpotential is up at 181 mV and the exchange current density is down to 0.82 $mA\,cm^{-2}$.

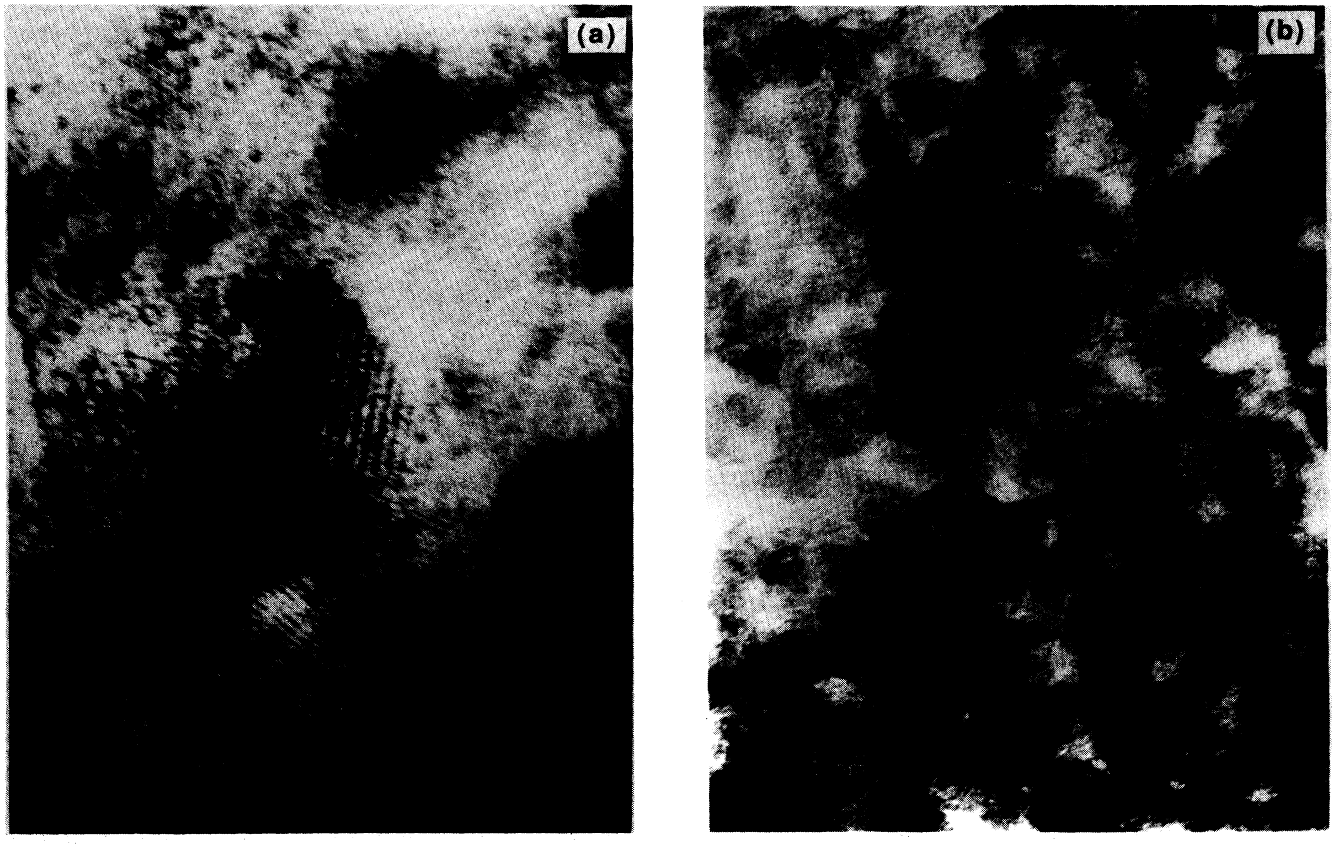

FIG. 8. TEM micrographs of $Fe_{66}Co_{18}Si_1B_{15}$ after (a) 8 h and (b) 25 h of milling.

The poor properties of the samples containing 26 at. % Co (samples *G* and *H*) may have several causes: sample *H* is partially crystalline in the as-prepared state as discussed previously, sample *G* contains larger crystals and some boride phases, or it may be that an optimum Co concentration exists in order to achieve the best electrocatalytic properties. More work is needed to answer these questions. The optimum properties were found for the 20 at. % Co alloys (samples *E* and *F*) in both forms: the activated ribbon as well as the nanocrystalline electrode made from powders milled for 8 h.

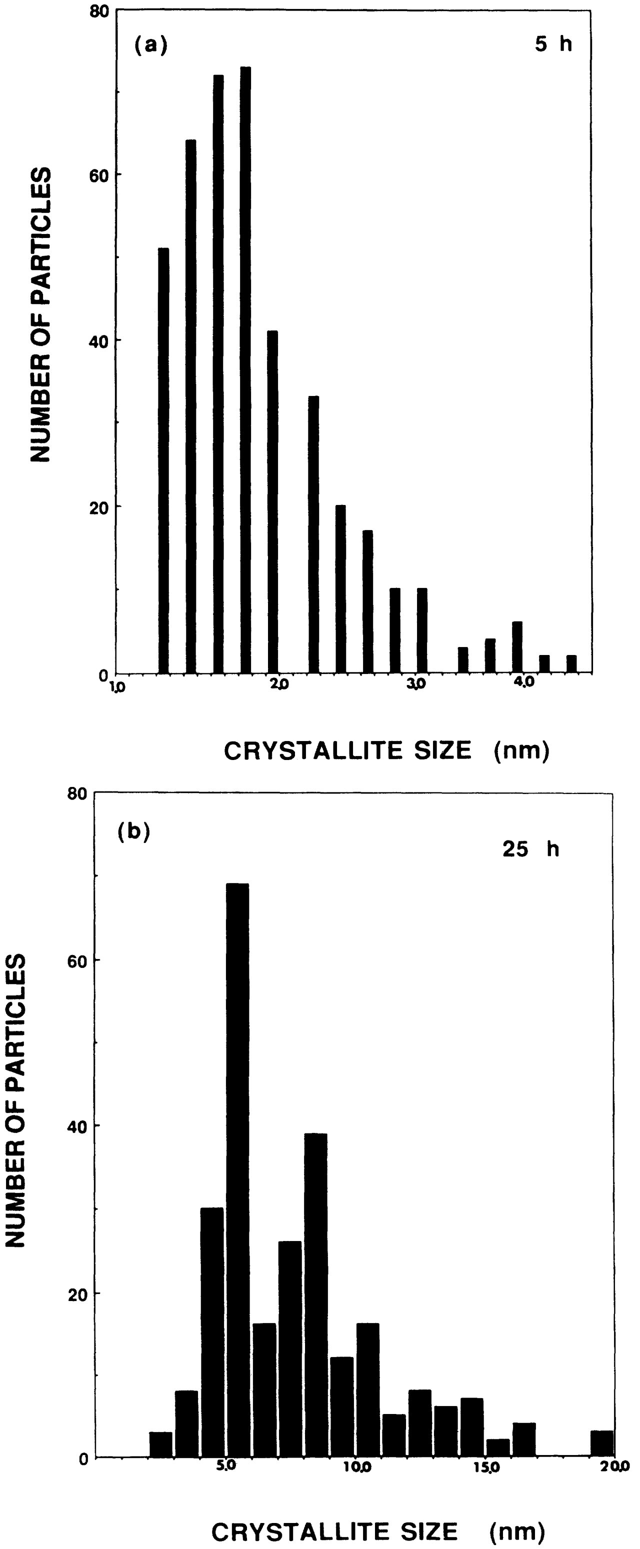

FIG. 9. Size distribution of the crystallites in $Fe_{66}Co_{18}Si_1B_{15}$ after (a) 5 and (b) 25 h of milling.

The effects of a prior *in situ* oxidation-reduction treatment on the electrocatalytic properties of some nanocrystalline powder electrodes were also investigated. Table II summarizes the results for samples *E* and *J* described in Table I. For the Co-based alloy, the treatment has basically no effect on the hydrogen overpotential (164 mV for the untreated nanocrystalline pellet versus 167 and 154 mV for the treated alloys at 1 and 10 mA cm^{-2}, respectively). These values are comparable to the 157 mV corresponding to the activated amorphous ribbon (sample *F* in Table I). The anodic oxidation treatment decreases, however, the exchange current density of the nanocrystalline electrode from 1.3 mA cm^{-2} (sample *E* in Table I) to 0.61 and 0.83 mA cm^{-2} (Table II).

For the Ni-based powder electrode, the oxidation-reduction process improves the catalytic properties. The overpotential decreases from 231 mV (sample *J* in Table I) to 211 and 187 mV and the exchange current density increases significantly from 0.25 mA cm^{-2} to 1.6 and 2.2 after 1 and 10 mA cm^{-2} of anodic current, respectively. The reason why the electrochemical oxidation-reduction treatment has such an effect on the Ni-based powder electrode but not on the amorphous ribbon (see sample *I* in Table I) is still unknown. The extremely small crystalline precipitates observed by TEM in the powder electrode or

FIG. 10. Dark-field micrographs of $Fe_{65}Ni_{17}Si_7B_{11}$ after 25 h of milling.

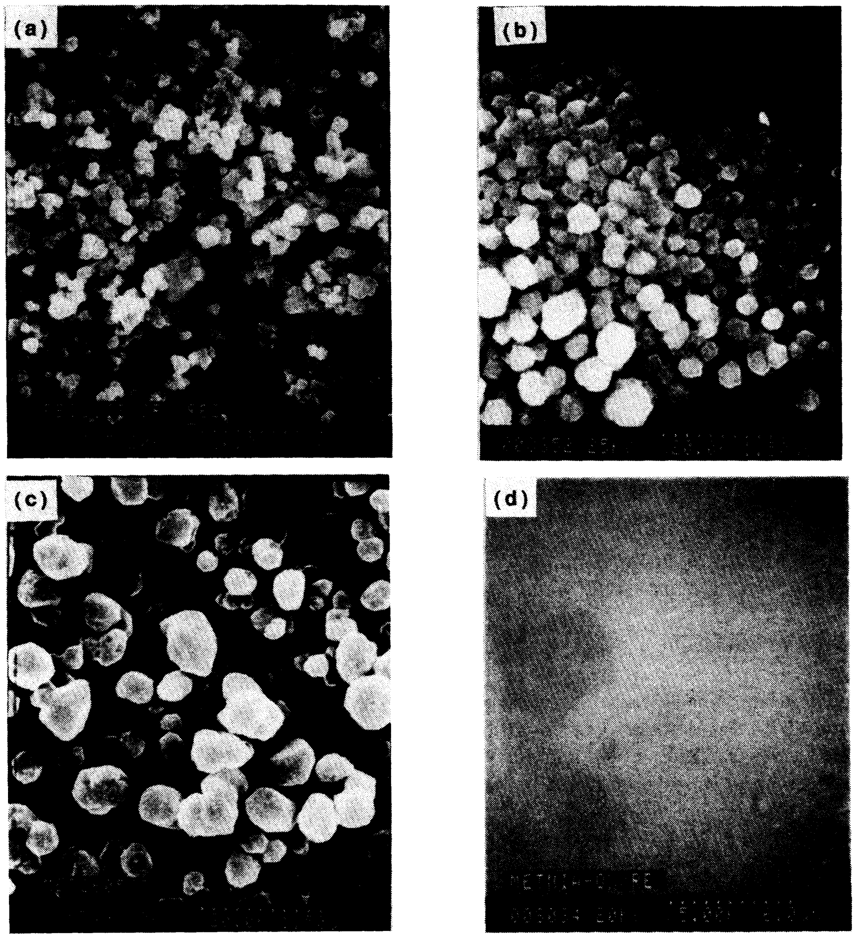

FIG. 11. Scanning electron micrographs of electrode (a) *F*, (b) *B*, (c) *D*, (d) *I* after the oxidation-reduction treatment.

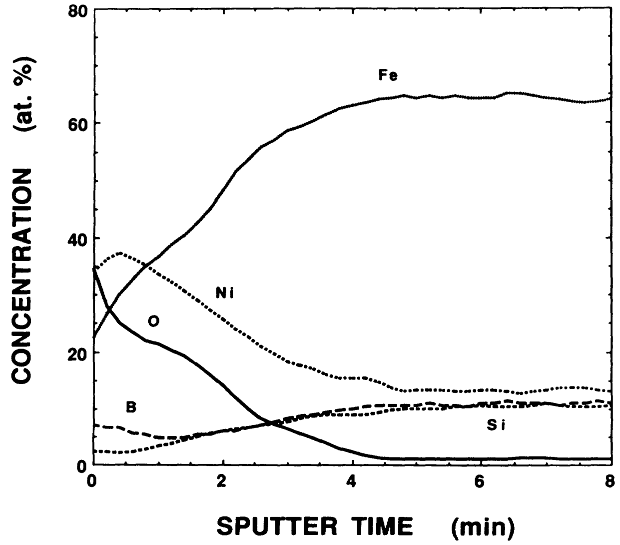

FIG. 12. Auger depth profile of the surface of $Fe_{65}Ni_{17}Si_{11}B_7$ after the oxidation-reduction treatment.

the presence of a large number of structural defects and a rough surface morphology may be at the origin of this phenomenon. The increased activity of the powder electrode after treatment could, for instance, be explained by the absence of a continuous passive Ni-oxide layer as in the case of the amorphous ribbon electrode.

IV. CONCLUSIONS

The Fe-(Co,Ni)-Si-B amorphous alloys crystallize when they are subjected to high-energy mechanical deformations. The presence of Co speeds up the precipitation process while Ni inhibits crystallization. The first phase which appears is α-iron followed by the crystallization of a boride phase. The crystal growth process is in direct competition with the mechanism of fracture of the crystals due to the accumulation of internal strain in the lattice. Because of both effects, the average crystallite size reaches, after a long milling time, an equilibrium value of about 8–10 nm. The study of the kinetics of the crystalline growth during mechanical crystallization reveals, contrary to the thermally activated crystallization process, a similar growth mechanism for both crystalline phases. Moreover, thermal analysis of the powders taken throughout the milling process shows a continuous change in the thermal growth mechanism as a function of milling time. The changes are related to the important microstructural modification induced by the high-energy mechanical deformations.

The electrocatalytic properties of the alloys for the H_2 evolution reaction in alkaline solutions reveal that the nanocrystalline cathodes are much more active than the non-treated amorphous ribbon counterparts. They have about the same level of activity as the ribbons with the same chemical composition after oxidation-reduction treatments. This is not surprising since both processes (the mechanical crystallization and the oxidation-reduction treatment) produce α-iron crystallites.

The process of mechanical crystallization is thus a powerful tool to produce extremely fine stable or metastable crystalline nanostructure. It allows a fine control of the crystal size distribution, the volume fraction of the various phases and, in some cases, the chemical composition of the material as well. It may be used effectively to produce highly electroactive materials.

---

[*] Present address: Centre de Technologie Noranda, 240 Hymus, Pointe-Claire, Québec, Canada H9R 1G5.

[1] H. E. Schaefer, R. Wurschiam, R. Birringer, and G. Gleiter, J. Less-Common Met. **140**, 161 (1988).

[2] R. Birringer, Mater. Sci. Eng. A **117**, 33 (1989).

[3] H. Gleiter and P. Marquart, Z. Metall. **75**, 263 (1984).

[4] S. J. Thorpe, B. Ramaswami, and K. T. Aust, Acta Metall. **36**, 795, (1988).

[5] Y. Yoshizawa, S. Oguma, and K Yamauchi, J. Appl. Phys. **64**, 6044, (1988).

[6] E. Hellstern, H. J. Fecht, C. Garland, and W. L. Johnson, *Symposium on Multicomponents Ultrafine Microstructures,* edited by L. E. McCandlish, B. H. Kear, D. E. Polk, and R. W. Siegel (Materials Research Society, Boston, MA, 1989), Vol. 132, p. 137.

[7] E. Hellstern, H. J. Fecht, Z. Fu, and W. L. Johnson, J. Appl. Phys. **65**, 305 (1989).

[8] M. L. Trudeau, J. Y. Huot, and R. Schulz, Appl. Phys. Lett. **58**, 2764 (1991).

[9] M. L. Trudeau and R. Schulz, Mater. Sci. Eng. A **134**, 1361 (1991).

[10] J. Y. Huot, M. L. Trudeau, and R. Schulz, J. Electrochem. Soc. **138**, 1316 (1991).

[11] M. L. Trudeau, D. Dussault, A. Van Neste, and R. Schulz, Phys. Rev. Lett. **64**, 99 (1990).

[12] J. Y. Huot, M. L. Trudeau, L. Brossard, and R. Schulz, J. Electrochem. Soc. **136**, 2224 (1989).

[13] M. L. Trudeau, J. Y. Huot, and R. Schulz, J. Appl. Phys. **67**, 2333 (1990).

[14] T. Nakajima, E. Kita, and H. Ino, J. Mater. Sci. **23**, 1279 (1988).

[15] G. Cliff and G. W. Lorimer, J. Microsc. (Oxford) **108**, 203 (1975).

[16] S. F. Bartram, in *Handbook of X-Rays,* edited by E. F. Kaelble (McGraw-Hill, New York, 1967), p. 17-1.

[17] J. W. Christian, in *The Theory of Transformations in Metals and Alloys, Part I,* 2nd ed., edited by D. W. Hopkins (Pergamon, Oxford, 1981).

[18] G. A. Jones, P. Bonnett, and S. F. H. Parker, J. Mag. Mag. Mater. **58**, 216 (1986); G. A. Jones, S. F. H. Parker, and S. D. Eyres, *ibid.* **67**, 167 (1987).

[19] G. O. Piloyan, Nature (London) **10**, 1229 (1986).

[20] These values were obtained by taking into account the small variations in the activation energy for thermal crystallization during the milling process. The activation energy of 3.5 eV found for the ribbon drops progressively to 2.8 eV after 15 h of milling.

[21] E. Hellstern and L. Schultz, J. Appl. Phys. **63**, 1408 (1988).

[22] T. G. Richards and G. P. Johari, Philos. Mag. B **58**, 445, (1988).

[23] U. Mizutani and C. H. Lee, J. Mater. Sci. **25**, 399 (1990).

[24] M. L. Trudeau, A. Van Neste, and R. Schulz, in *Clusters and Cluster-Assembled Materials,* edited by R. S. Averback, D. L. Nelson and J. Bernholc, MRS Symposia Proceedings (Materials Research Society, Pittsburgh, 1991), Vol. 206, p. 487.

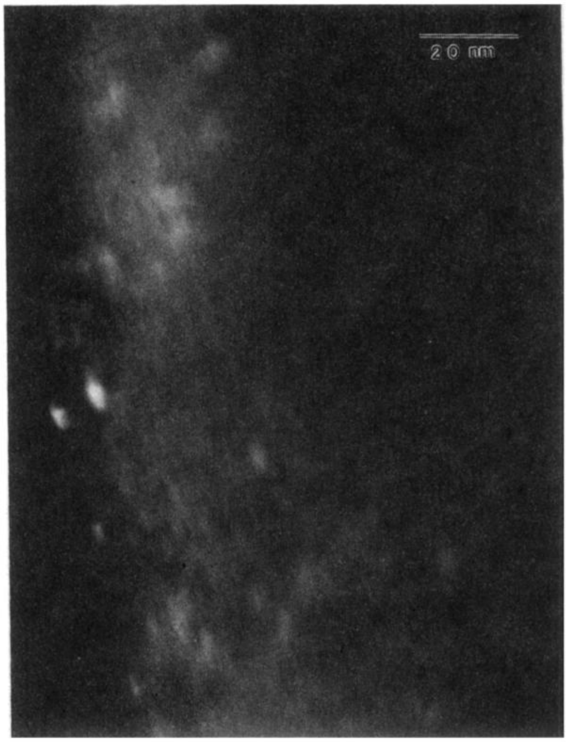

FIG. 10. Dark-field micrographs of $Fe_{65}Ni_{17}Si_7B_{11}$ after 25 h of milling.

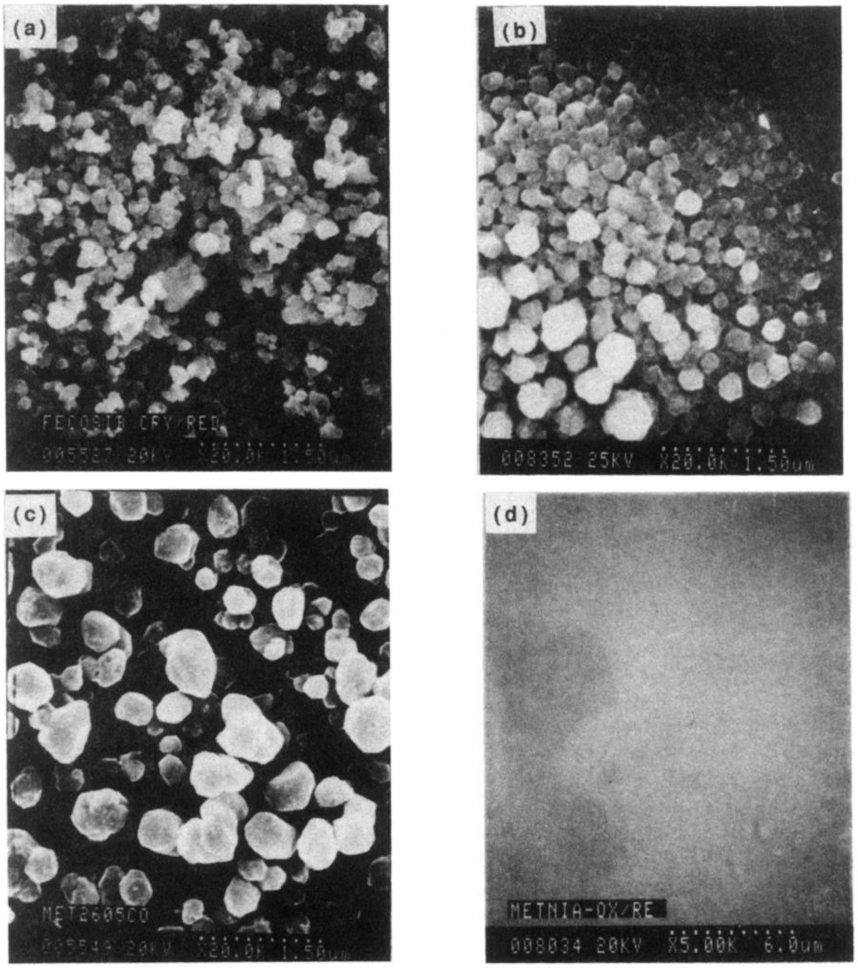

FIG. 11. Scanning electron micrographs of electrode (a) *F*, (b) *B*, (c) *D*, (d) *I* after the oxidation-reduction treatment.

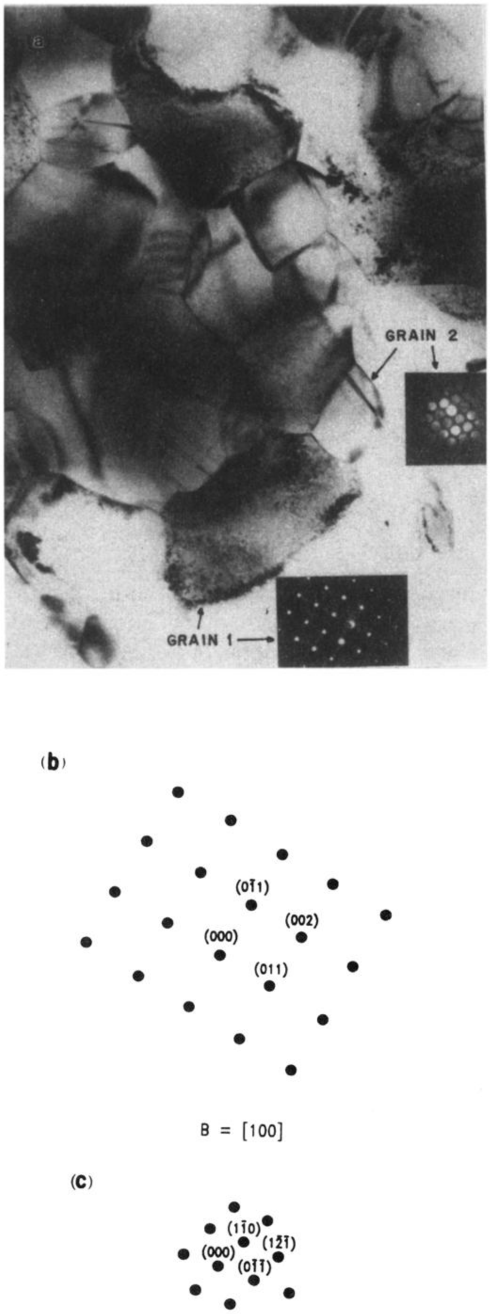

FIG. 2. (a) TEM micrograph of crystalline $Fe_{60}Co_{20}Si_{10}B_{10}$ alloy. (b) and (c) Schematic diffraction patterns of the grains shown in (a).

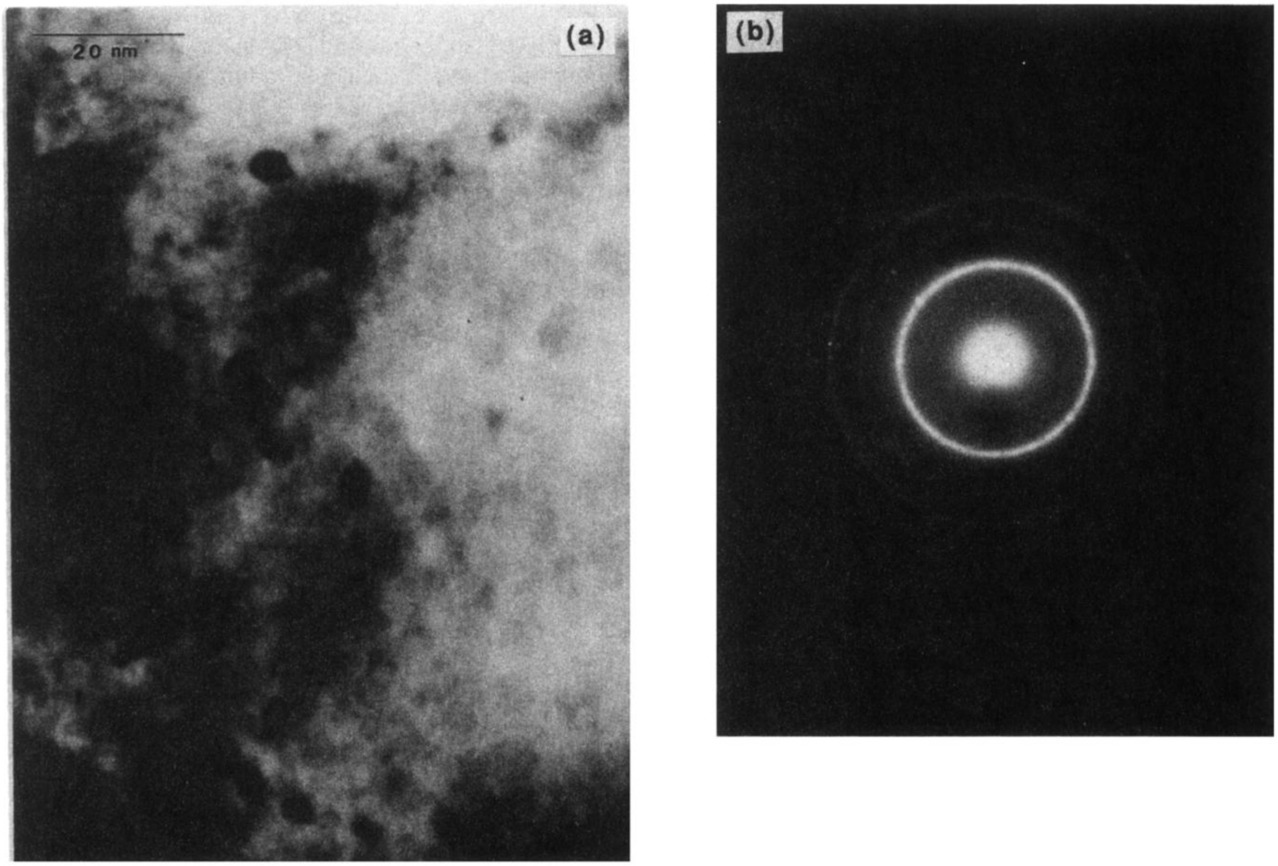

FIG. 7. (a) Bright-field micrographs and (b) electron-diffraction pattern of $Fe_{66}Co_{18}Si_1B_{15}$ after 3 h of milling.

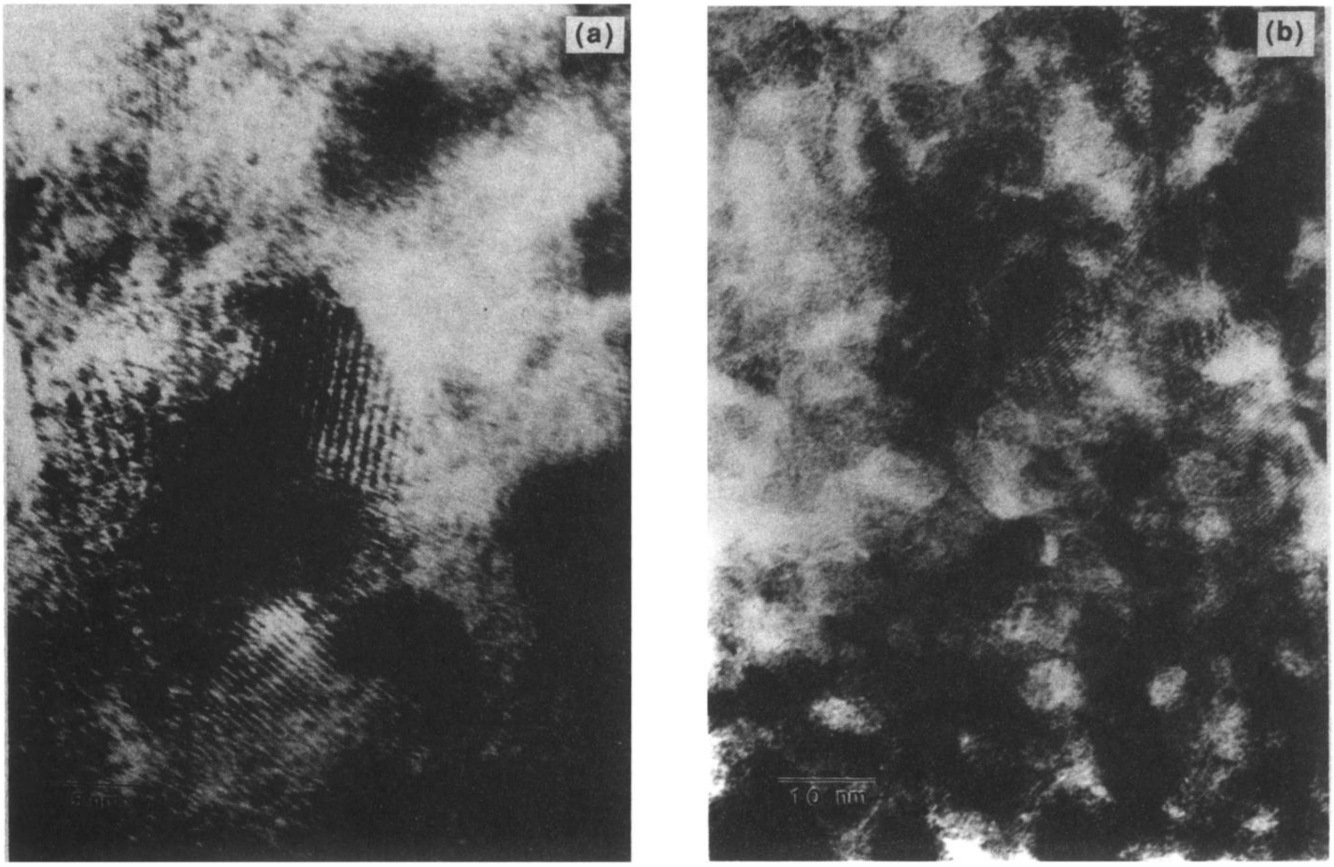

FIG. 8. TEM micrographs of $Fe_{66}Co_{18}Si_1B_{15}$ after (a) 8 h and (b) 25 h of milling.